Biomass and Bioenergy 119 (2018) 346–353

Contents lists available at ScienceDirect

Biomass and Bioenergy

journal homepage: www.elsevier.com/locate/biombioe

Research paper

How and why does willow biochar increase a clay soil water retention capacity?

Kimmo Rasa[a,*], Jaakko Heikkinen[a], Markus Hannula[b], Kai Arstila[c], Sampo Kulju[a], Jari Hyväluoma[a]

[a] Natural Resources Institute Finland, Luke, FI-31600, Jokioinen, Finland
[b] BioMediTech Institute and Faculty of Biomedical Sciences and Engineering, Tampere University of Technology, FI-33101, Tampere, Finland
[c] University of Jyvaskyla, Department of Physics, P.O. Box 35, FI-40014, Finland

ARTICLE INFO

Keywords:
Biochar
X-ray tomography
3D image analysis
Helium ion microscopy
Soil water retention
Plant available water

ABSTRACT

Addition of biochar into a soil changes its water retention properties by modifying soil textural and structural properties. In addition, internal micrometer-scale porosity that is able to directly store readily plant available water affects soil water retention properties. This study shows how precise knowledge of the internal micrometer-scale pore size distribution of biochar can deepen the understanding of the biochar-water interactions in soils. The micrometer-scale porosity of willow biochar was quantitatively and qualitatively characterized using X-ray tomography, 3D image analysis and Helium ion microscopy. The effect of biochar application on clay soil water retention was studied by conventional water retention curve approach. The results indicate that the internal pores of biochar, with sizes of at 50 and 10 μm (equivalent pore diameter), increased soil porosity and the amount of readily plant available water. After biochar addition, changes in soil porosity were detected at pore size regimes 5–10 and 25 μm, i.e. biochar pore sizes multiplied by factor 0.5. The detected pore size distribution of biochar does not predict directly (1:1 compatibility) the changes observed in the soil moisture characteristics. It is likely that biochar chemistry and pore morphology affect biochar-water interactions via e.g. surface roughness and contact angle. In addition, biochar induced changes in soil structure and texture affected soil moisture characteristics. However, the approach presented is an attractive pathway to more generalized understanding on how and why biochar internal porosity affects soil moisture characteristics.

1. Introduction

While biochar is considered as a potential measure to sequester carbon into soil [1], its secondary effects on soil properties are often controversial [2]. Biochar has been shown to increase soil water holding capacity (WHC), but no solid understanding exists on the effects of, e.g., soil type, biochar quality or climate. Addition of biochar into a given soil changes soil textural and structural properties. These changes modify soil moisture characteristics in a specific manner depending on biochar type and soil properties (indirect mechanism). However, biochar as a highly porous material also directly affects soil water holding capacity via its internal porosity. The aim of this paper is to study how this internal porosity and pore size distribution are related to the amount of plant available water in a clay soil.

A large number of papers describe biochar effect on soil hydraulic properties and water holding capacity [3–6] with heterogeneous descriptions of biochar physical quality. Physical characteristics of biochar is most commonly studied by gas adsorption techniques accompanied by the Brunauer-Emmett-Teller (BET) modelling to determine the specific surface area [7] or Barrett-Joyner-Halenda (BJH) modelling to determine pore size distribution [8]. However, pore space analysis based on gas adsorption measurements is limited to pores smaller than 300 nm, whereby it does not tell much about the porosity in the size range that is important for plant water uptake (i.e. micrometer-scale pores).

The inadequacy of gas adsorption studies and drawbacks related to porosity measurements using mercury porosimetry have been addressed in earlier studies [9,10]. NMR Cryoporometry have also been used to study porous materials at nanometer length-scale, however, resolution in the upper end is limited to few micrometers [11]. Kinney et al. [4] addressed the need for quantitative techniques to characterize micrometer-scale pores within the biochars due to their expected importance on soil WHC. All these studies support theory that large internal micrometer-scale pores of biochar may have remarkable direct

* Corresponding author. Natural Resources Institute Finland, Luke, Production systems, Biorefinery and Bioproducts, Finland.
E-mail address: kimmo.rasa@luke.fi (K. Rasa).

https://doi.org/10.1016/j.biombioe.2018.10.004
Received 21 December 2017; Received in revised form 28 September 2018; Accepted 2 October 2018

effect on soil moisture characteristics (indirect effect refers to changes in soil texture and formation of soil aggregates through bindings between biochar and soil particles, see Ref. [12]). However, the effect of biochar micrometer-scale porosity on soil moisture characteristics has not been quantitatively analysed.

We anticipate that the way forward in increasing understanding of biochar-water interactions goes through fundamental research on internal pore structure of biochars. Lately, X-ray tomography and 3D image analysis methods have been adapted to biochar research. This approach is able to visualize the internal pore structure of biochar, and to directly determine pore characteristics such as pore size distribution and pore continuity. In recent studies X-ray tomography has been used to characterize pore structure of biochars derived from various raw materials (e.g. *Pinus sylvestris*, *Miscanthus, Populus spp. L.,* cottonseed hull, hay) with resolution ranging from 0.74 to 21 μm [13–17]. Hyväluoma et al. imaged various types of biochars and hydrochars with ca. 1 μm resolution and found that considerable part of the biochar volume consist of pores in size range relevant to hydrological processes and storage of plant available water [18]. In addition, they found high variation in porosity, pore size distribution and structural anisotropy between different biochars. Also aggregates of biochar-amended soil have been imaged with X-ray tomography, although at this length-scale X-ray tomography resolution cannot capture the internal porosity of biochar [19].

The lack of precise data on micrometer-scale porosity might be one reason that the importance of biochar internal porosity directly affecting the soil water holding capacity has been overlooked. In this study we used X-ray microtomography, 3D image analysis and Helium ion microscopy to study structural properties of willow biochar with emphasis on micrometer-scale pores contributing to storage of plant available water. Further, we conducted an incubation experiment to study the effect of this specific biochar on soil moisture characteristic and to identify pore regimes altered by biochar amendment. The relationship between biochar pore system and its specific effect on soil moisture characteristics is an attractive pathway towards development of precisely tailored biochars aimed to enhance water use efficiency.

2. Materials and methods

2.1. Experimental soil

Soil for incubation experiment was taken from Kotkanoja long-term drainage experiment site [20] located in Jokioinen in southern Finland (N 60.82°, E 23.51°). The study material was collected from the topmost 10 cm layer of an annually ploughed plot in spring 2016. The heavy clay soil had 64.8%, 30.5% and 4.7% of clay, silt and sand, respectively (mass fractions determined by pipette method [21]). Soil organic matter content was 9.2% (loss of ignition at 550 °C), carbon content 2.9% (Leco analysator), pH 6.3 and electrical conductivity 63.1 μS cm^{-1} (soil to water ratio 1:5).

2.2. Biochar

The biochar used in the experiment was pyrolysed in an indirectly heated pilot-scale batch-type pyrolysis facility using Willow stem wood (Salix sp, with bark) as raw material. Temperature profile of pyrolysis process consisted of two steps. First, the temperature was raised to 280 °C, and then further to 320 °C with rates of 2.2 and 0.2 K min^{-1}, respectively.

The elemental analysis (CHNSO) of biochar was carried out using FLASH 2000 series analyser and the results were used to calculate O:C and H:C atomic ratios. The biochar was analysed for pH (SF EN 13037, 1:5 char to water ratio), electrical conductivity (EC, SF EN 13038, 1:5 char to water ratio), nutrients and heavy metals (SFS-EN 13650 Aqua Regia extraction and ICP-measurement), BET surface area (ISO 9277:2010(E) Brunauer–Emmett–Teller (BET) Surface Area) and Ash content (SFS 3008, loss of ignition at 550 °C).

The BET surface area of biochar produced was 6.8 ± 0.43 $m^2 g^{-1}$. The elemental mass fractions of C, H, N, S and O were 74.0 ± 0.0%, 4.1 ± 0.1%, 0.4 ± 0.0%, 0.0 ± 0.0% and 15.8 ± 0.3%, respectively. The ash mass fraction of the biochar was 3.13 ± 0.15%. The corresponding mole ratios of H:C and O:C were 0.66 and 0.16, respectively. Biochar had low content of main nutrients (1.5 g kg^{-1}, 3.6 g kg^{-1}, 9.1 g kg^{-1} of P, K, Ca respectively) and heavy metals Cd, Cu and Pb (0.79 mg kg^{-1}, 6.8 mg kg^{-1}, < 3 mg kg^{-1}, corresponding limits are 1.5, 600 and 100 mg kg^{-1}, respectively) contents were below limits set for soil amendments in Finland.

2.3. X-ray tomography

The X-ray computed microtomography imaging was conducted with Zeiss Xradia MicroXCT-400 (Zeiss, Pleasanton, CA, USA) device. Source voltage was 40 kV and source current was 250 μA. The pixel size was 1.14 μm. A 20× objective was used with 2 binning. 1600 projections were taken in full 360°. Each projection was exposed with X-rays for 3 s. No filters were used in the imaging process. Zeiss XMReconstructor software with the filtered back projection algorithm was used in the reconstruction of the image stacks.

For quantitative structural analysis the original grey-scale image was de-noised and segmented into solid and void phases. Details of these image processing steps have been described by Hyväluoma et al. [18] and reviewed in Appendix A. The subvolume used in the further image analysis consisted of $1.9 \cdot 10^8$ voxels (sample size ca. 0.5 mm).

The porosity of the sample was calculated by dividing the number of void voxels by the total number of voxel in the analysed volume. The pore-size distribution was determined using an approach based on mathematical morphology [22] by successively applying morphological opening operations (sphere with radius r was used as the structuring element) on the pore space [23]. The pore size based on morphological opening closely relates to the stationary distribution of wetting and nonwetting fluids in pore space and the related capillary pressure via the Young-Laplace equation

$$p_c = \frac{2\gamma cos\theta}{r} \quad (1)$$

where γ is the surface tension, θ the contact angle, and r the pore radius defined as the radius of the structuring element used in the morphological opening [24]. This method is particularly suitable for our purposes where the pore-size distribution determined from imaged pore space is linked to measured soil moisture characteristic curve. The structural anisotropy of the sample was quantified by calculating the degree of anisotropy using the method based on grey-scale gradient tensor [25].

2.4. Helium ion microscopy

Helium ion microscopy (HIM) is a novel development within the family of scanning beam microscopes. Instead of using electrons for beam particles, as in conventional scanning electron microscopes (SEM), helium ions are used. Helium ions have a focal depth that is 5–10 times larger than electrons in SEM, a beam spot size below 0.5 nm, and very small interaction volume producing secondary electrons, resulting in images with very high resolution. Another important advantage of HIM is its capability to image insulating materials without charging effects (no metal coating is needed) as the positive surface charging from helium ions and secondary electrons can be neutralized with an electron flood gun. A Zeiss Orion NanoFab Helium ion microscope was used in this work.

2.5. Soil sample preparation

Experimental soil was air-dried in room temperature and sieved

through 6 mm mesh. Four different kinds of samples were prepared for incubation experiment. Half of the samples had natural (NAT) aggregate structure (< 6 mm). The soil for other half was homogenized (HOM) using a roller-mill and then sieved (2 mm) in order to destroy soil macro aggregates. Samples with NAT and HOM structure received 0% or 5% mass fraction biochar amendment (on dry matter basis). Biochar used in the experiment was crushed into fine powder using blender. Altogether 14 samples were prepared.

The incubation experiment was conducted in 190 cm^3 (7.1 cm in diameter) metal cylinders. One end of each cylinder was covered with a thin fabric to prevent sample to loss from the cylinder. The cylinders were filled with soil or mixture of soil and biochar. The samples were gently shaken and pressed using 10 kg weight. Finally, the excess material was removed by spatula.

2.6. Incubation

Soil samples were saturated with water for six weeks. Saturated samples were moved to sandbox (Eijkelkamp) and the matric potential was gradually adjusted to −10 kPa. Thereafter, the samples were incubated under constant matric potential (−10 kPa) and temperature (5 °C) conditions for six weeks. Cool incubation temperature was used to hinder the microbial activity in the samples.

2.7. Soil moisture characteristic curve

Volume fraction of soil water in matric potential range from −0.3 to −10 kPa was determined using sandbox (Eijkelkamp), whereas pressure plate extractor (Soilmoisture Equipment Corp.) equipped with 100 kPa, 300 kPa bar and 500 kPa ceramic plates was used to produce lower matric potentials. In each step the soil samples were let to equilibrate before determination of the water content. The lowest matric potentials −1500 kPa and −4000 kPa, were created osmotically by placing 1 g soil sample into desiccators equipped with containers with saturated solutions of ammonium oxalate ($(NH_4)_2C_2O_4$) or sodium chloride (NaCl), respectively. Thereafter the samples were removed from desiccators and the water content of the samples were determined by weighing the samples before and after drying them at 105 °C. Equilibration time varied between 1 day (at −0.3 kPa) and 6 weeks (at −1500 and −4000 kPa) depending on the matric potential.

2.8. Effect of biochar amendment on soil porosity

Data used to determine the soil moisture characteristic curve (SMC) was also used to study the effect of added biochar on the pore size distribution (See Eq (2). below). However, instead of using volume fraction of soil water, the water contents were expressed as ratio of water volume to dry mass of sample. This ratio was used to ensure that results contain only the pore volume related to biochar for each pore size interval. First, the soil water potentials were converted to approximate pore sizes using the Young-Laplace equation (Eq. (1)). While Young-Laplace equation is derived for straight capillaries with circular cross section and does not directly apply to soils with more complex pore geometry, it can be used to determine so-called equivalent pore diameter (EPD) d = 2r. Then, the water contents of the samples were interpolated on 2.75 µm pore size interval using linear interpolation. This increment corresponds to the increment in size of structure element used in determination of pore size distribution from tomography images.

Finally, the effect of biochar on soil porosity was calculated as follow:

$$\Delta v_{[p,p-\Delta p]} = (W_p - W_{p-\Delta p})/M_{5\%} - (W_p - W_{p-\Delta p})/M_{0\%}, \quad (2)$$

where Δv is the effect of biochar amendment on specific pore volume of soil in each pore size interval (cm^3/g), W is the volume fraction of soil water of the sample (= pore volume, cm^3), M is the dry matter weight of the sample (g), p is the upper limit and p-Δp lower limit of pore size interval (p = 2.75 µm, 5.5 µm, …; Δp = 2.75 µm) and $^{<>}{}_{5\%}$ and $^{<>}{}_{0\%}$ represents the average of the samples with and without biochar. Calculation was performed separately for two different soil structures (HOM, NAT).

2.9. Statistical analysis

The dependence of plant available water on the biochar addition and soil structure was studied using two-way analysis of variance. Dependent variables were proportions (values between 0 and 1) and therefore logit transformation was used to make the model assumption applicable. For the presentation of the results, the estimated means were transformed back to the original scale. Bonferroni correction was applied to multiple comparisons. All statistical analyses were performed using Matlab with Statistics Toolbox.

3. Results and discussion

3.1. X-ray tomography of willow biochar

The visual observation of the X-ray tomography image revealed that the pore structure of willow biochar pyrolysed at 320 °C retained the initial structural characteristics of fresh stem wood (Fig. 1). Obviously, the vascular tissues (xylem) in sapwood and/or heartwood appear as biochar porosity. Analogously to living wood tissue, these pores are

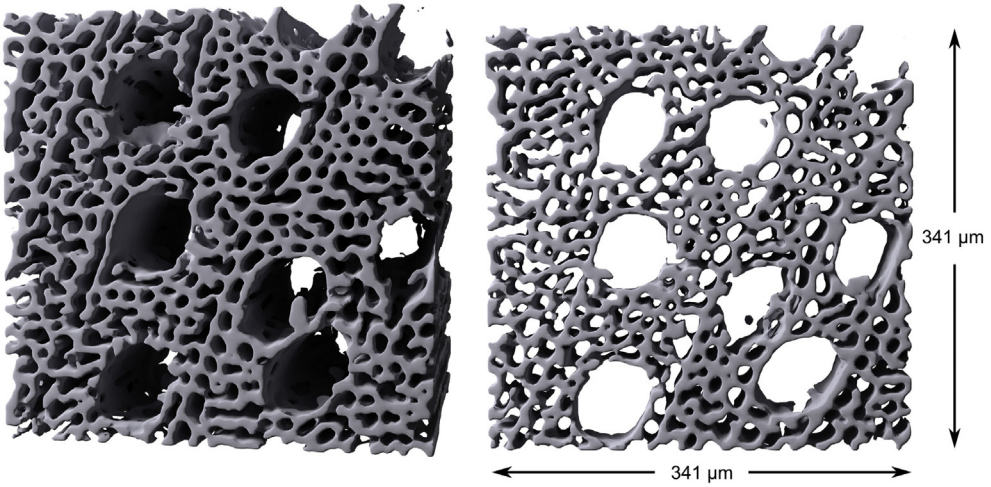

Fig. 1. X-ray tomographic reconstruction of willow biochar (left). The 3D visualization of tomography data was produced with Paraview [29] and Blender. The tomography data consisting of the imaging slices were first rotated with ImageJ [30] in a way that pores are perpendicular to the cutting face. After this a cuboid piece was cut from a sample. A 57 µm thick slice cut from the middle of a cuboid piece is shown on right.

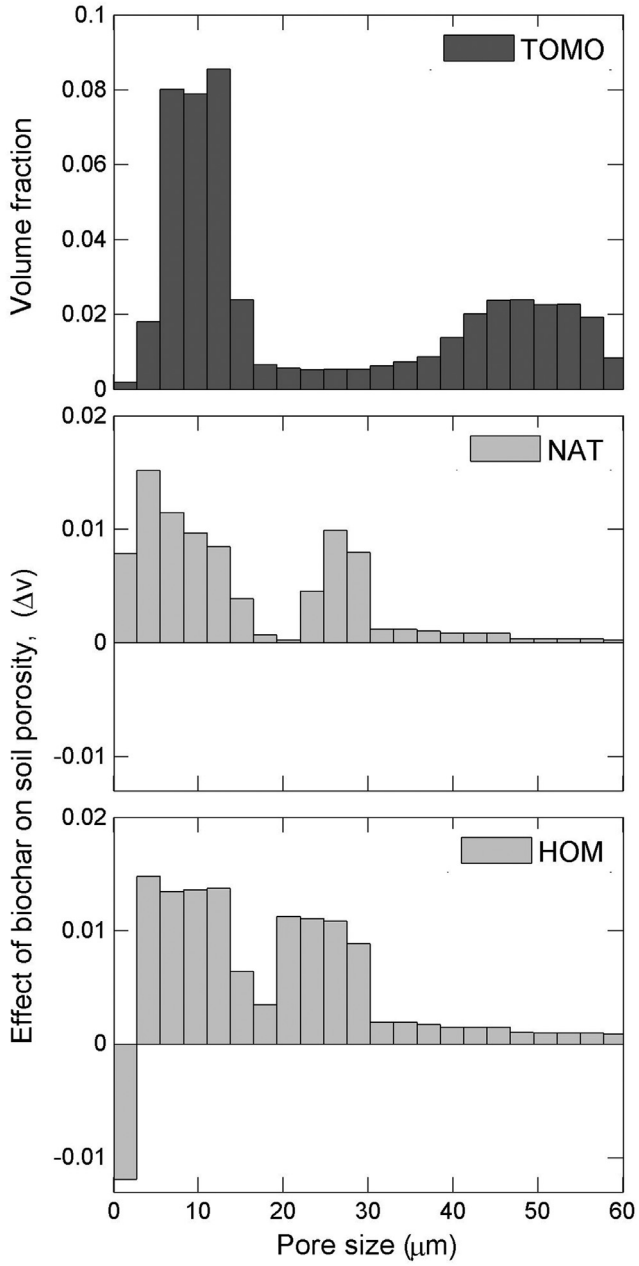

Fig. 2. Pore size distribution determined by 3D image analysis of X-ray tomography image (top panel) and the change in the pore size distribution due to biochar addition for NAT (middle panel) and HOM (bottom panel) samples. Effect of biochar on soil porosity (Δv, $cm^3\ g^{-1}$ soil) was determined by subtracting the soil water content (expressed as a ratio of water volume to dry mass of sample) of pure soil from that of soil-biochar mixture as described in Sec. 2.8. Matric potential was converted to equivalent pore size using Eq. (1).

mainly responsible for water storage and transport within the biochar.

The biochar pore system was quantified by image analysis of the X-ray tomography image. The results show that the total porosity of biochar is 0.6 and the pore size distribution is bimodal with local maxima around diameters 10 and 50 μm (Fig. 2 top panel). The degree of anisotropy was 32.0 (see Hyväluoma et al. [18] for reference values of degree of anisotropy for several wood based biochars) which proves that porosity of the biochar is highly anisotropic and consists of parallel cylindrical pores with minimum number of lateral connections (verified by HIM, see below). In general, these findings are well in line with earlier published 2D scanning electron microscopy images indicating bimodal characteristics of fresh willow wood structure e.g. Refs. [26,27]. In addition, a recent paper [28] discussing the effect of pyrolysis temperature on micrometer-scale porosity of willow (Salix schwerinii 'Amgunskaja') biochar shows similar bimodal pore characteristics as in the present paper.

The used imaging resolution prevents observation of pores in submicrometre size range. However, the low BET surface area ($6.8 \pm 0.43\ m^2\ g^{-1}$) suggests poorly developed nanoporosity of the studied biochar. This suggestion is in line with previous studies reporting development of pyrogenetic nanopores only in higher pyrolysis temperatures [10,31,32]. To verify this hypothesis, we studied nanoporosity of biochar pore walls using HIM, which indicated that cell wall structures remaining in the biochar do not contain visible nano-scale pores (Fig. 3). HIM observations and degree of anisotropy together suggest that water storage and flow within willow biochar takes place in "bundle of cylindrical capillaries" as is assumed in Eq. (1) (see also discussion in Sec. 3.3).

3.2. Effects of biochar amendment on soil-moisture characteristics

Addition of biochar reduced the bulk density of NAT (from 0.91 to $0.87\ g\ cm^{-3}$, $P = 0.001$) and HOM (from 1.08 to $0.93\ g\ cm^{-3}$, $P < 0.001$) samples compared to samples without biochar. The effect was more pronounced in HOM samples, because in HOM samples biochar replaces more mineral soil than in the case of NAT. In NAT samples biochar falls partially in pores between aggregates and thus affects the soil bulk density less. These indirect effects of biochar amendment explain changes observed in the wet-end of SMC (related to pores with larger size than the size of internal pores of biochar, see below).

Biochar application influenced soil moisture characteristics over the entire range of measured matric potentials. The major changes occurred at matric potentials above −316 kPa, while differences levelled out at the dry-end of the curve (Fig. 4). According to Young-Laplace equation, in matric potential of −300 kPa water remaining in soil is stored in pores with EPD < 1 μm. Biochar addition thus modifies soil porosity especially at pore size regime EPD > 1 μm. In general, this finding indicates that biochar with high micrometer-scale porosity, observed with X-ray tomography and 3D image analysis, reflects directly to soil WHC in regime important for plant water uptake (Fig. 4, Table 1).

Closer inspection of SMC for NAT and HOM samples (Fig. 2) reveals that biochar application increased porosity in two specific regimes. In both soils (irrespective of soil structure), a clear increase in porosity occurred at pore sizes around 25 μm (EPD). The other maximum is approximately at EPD 5 μm and 10 μm for NAT and HOM samples, respectively. These peaks correspond the pore sizes observed in the biochar (10 and 50 μm, EPD) multiplied by factor 0.5 for larger pores. This factor differs slightly between NAT and HOM samples for smaller pore class. The fact that a bimodal shape is observed both in the pore-size distribution determined with image analysis and derived from SMC provide strong support for the inference that biochar affects the soil moisture characteristics greatly via direct mechanism. In next section some biochar-related properties affecting how biochar internal porosity translates to changes observed in SMC are discussed in more details.

3.3. Biochar pore sizes vs. changes in soil moisture characteristics

There are several reasons why it is unlikely that a one-to-one compatibility between 3D image analysis and SMC results will be obtained. Conversion of the SMC to porosity response curve was by using the Young-Laplace equation with generalized assumptions which are typically not fully valid for any practical porous material including the pore system considered here. One assumption is that pore space consists of a bundle of cylindrical capillaries with uniform circular cross section of different sizes and perfectly smooth surfaces. In addition it is assumed that pore walls are chemically homogeneous and perfectly wetting, i.e., in the Young-Laplace equation $\cos\theta = 1$ at all pore surfaces.

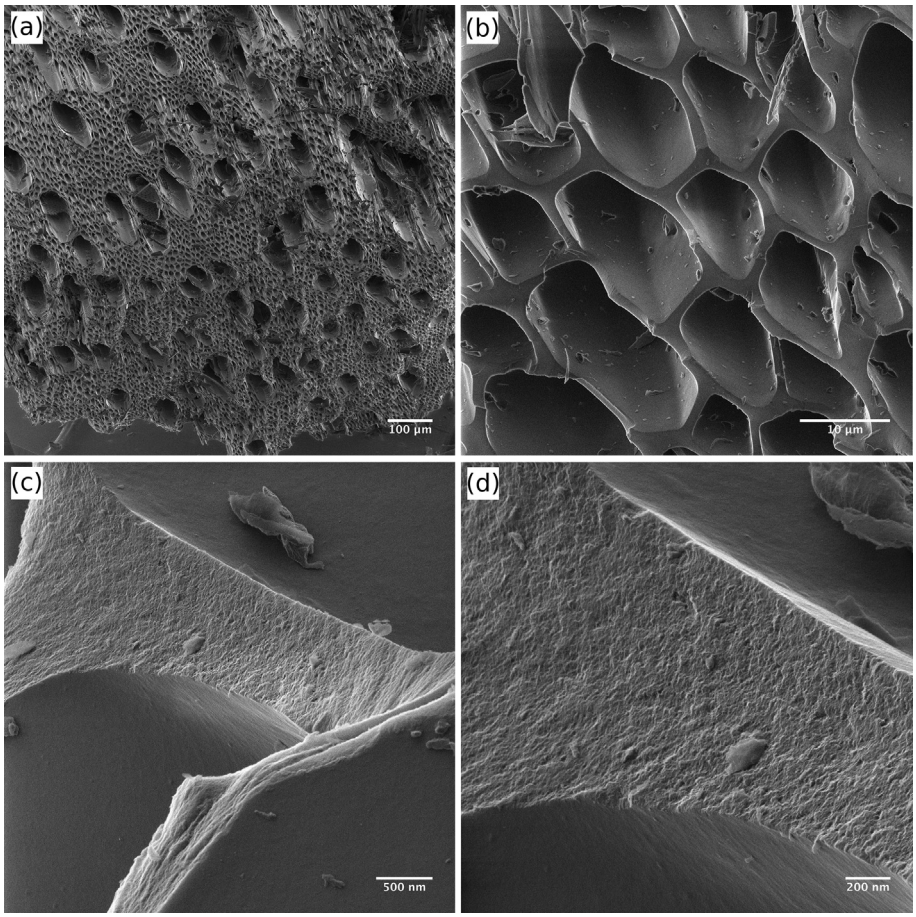

Fig. 3. Helium ion microscopy images of willow biochar. Size of the images (a) 1 mm, (b) 50 µm, (c) 4 µm, and (d) 2 µm. In image (a) overall porosity of biochar is shown while image (b) is focused on pores with EPD of approx. 5–10 µm. Image (c) shows pore wall between the biochar pores and (d) is the same pore wall with higher magnification indicating that there is no visible connections between individual pores.

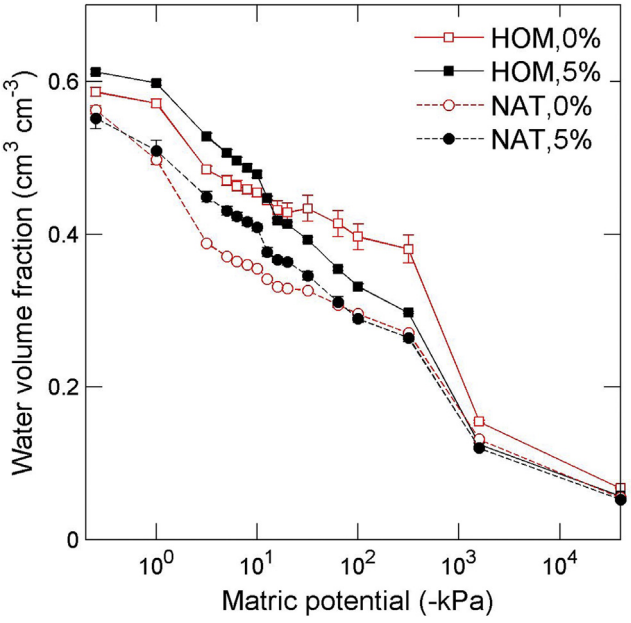

Fig. 4. Soil moisture characteristics curve for each studied soil structure and biochar combinations. Presented results are average of each treatments (n = 4 and n = 3 for samples with and without biochar addition, respectively). Error bars denote standard deviations.

Practically all pore surfaces are rough. Wenzel's model is widely used to describe the effect of surface roughness on the contact angle [33]. Another effect of surface heterogeneities is so-called contact angle hysteresis which means that contact angle is not unique but varies between two extreme values known as receding and advancing contact angles. Also, assumption of perfectly wetting pore walls is not realistic. To account for both non-perfect wetting and roughness, one can write

$$\cos\theta = r\cos\theta^* \quad (3)$$

where r is the roughness factor defined as the ratio of the true surface area to the apparent (projected) area and θ* is so-called intrinsic contact angle. In reality biochars are subcritically hydrophobic ($0^\circ < \theta^* < 90^\circ$) and pore surfaces rough, whereby $\cos\theta^* < 1$ and $r > 1$. Therefore, depending on the physical and chemical properties of pore walls, pore sizes can be either larger or smaller than those deduced from SMC. The importance of wetting properties on the hydrologic effects of biochar on soil has been demonstrated by Suliman et al. [34].

It must also be emphasized that simple approaches to wettability (including the discussion above) do not consider complicated time-dependent behavior observed in many natural systems. Wettability of many natural materials, including soil and biochar, is a highly complex phenomenon which is not yet properly understood.

In practice, it is difficult to determine the contact angle needed to properly use the Young-Laplace equation. The commonly used method that is based on optical determination of the contact angle for a sessile drop does not measure intrinsic contact angle as the measurement is performed on a rough surface of material. Sessile drop method has been used to determine contact angle for biochars [15,35]. It is important to note that this large-scale roughness does not correspond to the small-scale roughness used in Eq. (2). The intrinsic contact angle should be determined at the three-phase contact line within the pore which is not possible in practice. Furthermore, the derived roughness factor r in Eq. (2) is the roughness at pore walls which also is practically impossible to determine.

The discussion above explains the factors why there is not one-to-

Table 1
Water volume fraction at matric potential of −10 kPa (Field capacity, FC) and −1500 kPa (Permanent wilting point, PWP), plant available water (PAW) between these matric potentials and readily plant available water (RPAW) between matric potentials of −10Kpa and −316 kPa.

		FC (cm^3 cm^{-3})		PWP (cm^3 cm^{-3})		PAW (cm^3 cm^{-3})		RPAW (cm^3 cm^{-3})	
NAT	0%	0.36	$p < 0.001$	0.13	$p = 0.01$	0.22	$p < 0.001$	0.08	$p = 0.02$
	5%	0.41		0.12		0.29		0.14	
HOM	0%	0.45	$p = 0.04$	0.15	$p < 0.001$	0.30	$p < 0.001$	0.07	$p < 0.001$
	5%	0.48		0.12		0.35		0.18	

one correspondence between the pore sizes determined by image analysis and those derived from SMC. We also observed that there is different transform coefficient between the large pores and small pores. One explanation could be the existence of constrictions or throats in the biochar pores that could be formed, e.g., by tar compounds which could partially clog the pores.

Image analysis and porosity response derived from SMC can be directly compared only if all pores are connected to the sample surface directly or through larger pores. The Image analysis determines pore size distribution while SMC method is related to the size distribution of pore throats. Even though the pores in the used biochar were tubular and did not have obvious throats (see Secs. 3.1 and 3.2), we nevertheless estimated the effect of pore throats on the comparison by determining the throat size to pore size ratio using the method described in Appendix B.

In the analysis, we separated the two pore size classes present in the studied biochar by using pore diameter 25 μm as threshold between larger and smaller pores. The average throat size to pore size ratios were 0.97 and 0.78 for the larger and smaller pores, respectively. Thus for larger pores the throat effect was practically negligible while for smaller pores a clear effect was observed. This explains at least partly why the positions of modes related to smaller and larger pores are not shifted by same factor when comparing SMC results to pore size distribution determined by image analysis (Fig. 2).

Although the hypothetical consideration of biochar direct effect on the SMC is well established, the methodological limitations have hindered studies on this issue. However, the SMC results for sandy soils and SEM images of biochar presented by Abel et al. [36] could possibly be interpreted in similar way than in our study. Liu et al. found that biochar amendment shifted soil pore size distribution toward smaller pores, but biochar effect was not unambiguously established [5].

In addition to the direct influence of biochar internal pore system, biochar affects soil moisture characteristics via indirect mechanisms, i.e. soil-biochar interactions affecting soil structure (aggregate formation) and/or changes in soil particle size distribution [6,37]. The effect of soil structural changes probably explains why the modes of HOM treatment are wider than those of NAT treatment (Fig. 2). Interactions between soil-soil and soil-biochar are more common in HOM treatment with destroyed soil aggregates than in NAT treatment where biochar acts more independently in cavities between existing soil aggregates.

In any case, observed bimodal pore size distribution of willow biochar and consequent increase in soil water retention properties at corresponding pore size regimes (multiplied by factor 0.5) provides strong evidence that biochar internal micrometer-scale porosity contributes directly to soil water storage. This outcome encourages further studies and methodological development in order to improve understanding on relationship between biochar micron scale porosity and its direct effect on soil moisture characteristics.

3.4. Effects of biochar amendment on soil plant available water

Biochar application increased the plant available water (PAW) by 17% and 32% for HOM and NAT samples in comparison to samples with no biochar addition (Table 1). It is notable that in both studied soil structures the biochar induced increase in PAW occurred mostly matric potential regime from −10 to −316 kPa (Fig. 2), considered here as readily plant available water (RPAW), which corresponds to pores with EPD > 1 μm.

With respect to crop production at dry conditions and/or during vigorous growth, increased storage of RPAW helps plants to maintain potential transpiration rate for longer time. It is well documented that dry matter production of plants virtually ceases when they lose turgor pressure and this may occur far before permanent wilting point (PWP) [38]. Meyer and Green reported that wheat could use 52–57% of PAW before reduction in growth became evident [39]. In wider perspective, measures like biochar amendment to increase water productivity in agriculture (i.e. output yield per unit water used) are of importance in the struggle against water scarcity threatening global food security [40].

The present study highlights the importance of a direct link between the biochar micrometer-scale porosity and RPAW. Irrespectively to soil structure, biochar amendment increased soil porosity at the same pore size regimes (EPD 5–10 and 25 μm, Fig. 2), which refer to biochar induced changes via direct mechanism (biochar internal porosity). It could be hypothesized that this specific biochar would result in similar changes in other soil types as well. If the hypothesis holds, the approach presented above could provide a fascinating tool-box enabling development of tailored biochars that could modify soil moisture characteristics at well-defined moisture regimes over the range of soil types. Such tailored biochar products could improve biochar performance in crop production at different climatic areas, soil types and production systems, which is essential when sustainability of biochar is considered in global scale [1]. In any case, this hypothesis calls for further careful studies. However, it should also kept in mind that while biochar effects on SMC via direct mechanism may be independent of soil type, the biochar induced changes in soil bulk density, texture and structure are strongly depend on the properties of receiving soil and the type of biochar used.

4. Conclusions

The present study addresses the importance of biochar micrometer-scale porosity when used as soil amendment. It was shown that biochar internal porosity detected by X-ray tomography modifies SMC via direct mechanism. Bimodal porosity of willow biochar acted as traceable marker when added to a clay soil. However, a correction factor to predict relationship between biochar pore size distribution and its observed effects on SMC was needed (in this case close to 0.5) due to e.g. roughness and hydrophobicity of biochar pores. Because biochar was shown to increase soil porosity due to its internal porosity (direct mechanism) it could be hypothesized that this effect is independent from soil type. On the other hand, biochar induced changes in soil texture and structure, and modified SMC simultaneously (indirect mechanism). The latter mechanism is known to be strongly dependent on soil and biochar properties, which may explain why results on biochar effect on SMC are often controversial.

From the practical point of view, the willow biochar used in this experiment can greatly increase amount of readily plant available water (between matric potentials −10 and −316 kPa) in clay soil irrespective of soil initial structure. The result suggests that biochar amendment

would help plants to withstand moisture stress during dry periods and/or vigorous growth state. With respect to biochar use in growing media or agronomic applications, we strongly recommend utilization of research methods capable to reveal micrometer-scale pore structure of biochars.

Acknowledgements

Riikka Keskinen, Johanna Nikama and Ilkka Sarikka are warmly thanked for carrying out the laboratory work related to the soil moisture characteristic curve. We also wish to thank Mirja Muhola and Atte Mikkelson from VTT Technical Research Centre of Finland Ltd for carrying out BET surface area and CHNSO analysis. This project has received funding from the European Union's Horizon 2020 research and innovation programme under grant agreement No 637020 −MOBILE FLIP.

Appendix A

Image processing

Grey-scale X-ray tomography image was filtered with a three-dimensional median filter (radius 2). Filtered image was segmented into pore and solid voxels by global thresholding. Threshold value was selected with the modified Otsu's method [41] described Hyväluoma et al. [18]. This modified version utilizes ideas presented earlier by Hapca et al. [42]. Segmented image was then filtered with a majority filter (radius 2) and finally isolated ("floating") objects with volume less than 1000 voxels were removed from the image. A cross section of the grey-scale image and corresponding cross-section of the segmented and filtered image is shown in Fig. A1.

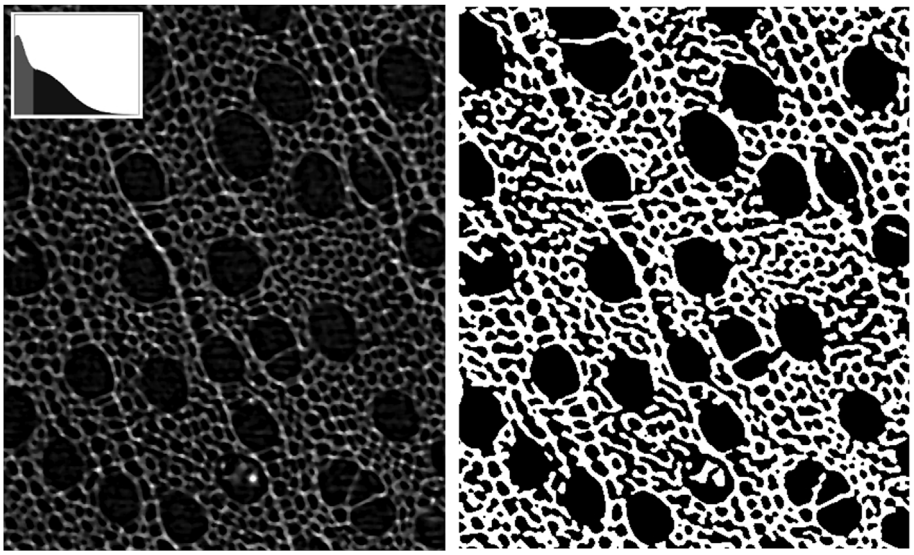

Figure A1. Cross sections of the x-ray tomography images of the willow biochar. On left, grey-scale image with grey-scale histogram in the inset. Lighter color in the histogram shows the grey-scale values interpreted as pore space and darker those interpreted as solid material. On right, final segmented and filtered image used in analyses.

Appendix B

Pore throat analysis

The ratio of pore size and the smallest throat leading to that pore was estimated in the following way. As a starting point, a tomographic image that was segmented into pores and solids was used. Method utilizes two scalar fields and one vector field derived from the image. First is distance transform which determines the shortest distance to the pore walls for each pore voxels. Distance transform was computed using so-called d [3–5,7] Chamfer metrics with a rescaling procedure as explained in detail by Svensson and Borgefors [43]. Secondly, for each voxel a pore size value was determined by morphological opening, e.g. Ref. [24]. Finally, we computed pore-scale flow field for saturated pressure-driven flow with driving pressure parallel with the pore direction. Here the lattice Boltzmann method was utilized for flow computation [44]. D3Q19 lattice Boltzmann model with two-relaxation time collision operator was used and the no-slip boundary condition at fluid-solid boundaries was enforced with bounce-back boundary condition. Sample size in the simulation was $454 \times 400 \times 638\,\mu m^3$. Further details of the used method can be found from, e.g., [45].

Throat size was then determined by utilizing distance transform, pore size and flow fields.

Inspection points were selected as local maxima of distance transform which were determined using a $5 \times 5 \times 5$ moving window. For these point, the streamlines were integrated both upstream and downstream, and the smallest pore size found following the streamline was then determined in both directions. As points along streamline do not coincide with the grid nodes, trilinear interpolation was utilized to determine the pore-size values. This method produces two throat sizes, one upstream and another downstream from the inspection point. Larger of these throats was selected as it is the easier route for the pore to be drained. The throat size thus determined is compared to the pore size at the inspection point to determine the throat to pore size ratio.

It should be noted that, as the tomography image used in this analysis is smaller than the grain size used in the experiment, the results obtained are only approximate. In real biochar grains routes to surface are longer and thus smaller throats could be present. Therefore, the results obtained can slightly underestimate the effect of pore throats.

References

[1] D. Woolf, J.E. Amonette, F.A. Street-Perrott, J. Lehmann, S. Joseph, Sustainable biochar to mitigate global climate change, Nat. Commun. 1 (56) (2010) 1–9 Nat. Commun.

[2] A. Mukherjee, R. Lal, Biochar impacts on soil physical properties and greenhouse gas emissions, Agronomy 3 (2014) 313–339.

[3] R.T. Barnes, M.E. Gallagher, C.A. Masiello, Z. Liu, B. Dugan, Biochar-Induced changes in soil hydraulic conductivity and dissolved nutrient fluxes constrained by laboratory experiments, PLoS One 9 (9) (2014) e108340, , https://doi.org/10.1371/journal.pone.0108340.

[4] T.J. Kinney, C.A. Masiello, B. Dugan, W.C. Hockaday, M.R. Dean, K. Zygourakis, R.T. Barnes, Hydrological properties of biochars produced at different temperatures, Biomass Bioener 49 (2012) 34–43.

[5] C. Liu, H. Wang, X. Tang, Z. Guan, B.J. Reid, A.U. Rajapaksha, Y.I. Ok, H. Sun, Biochar increased water holding capacity but accelerated organic carbon leaching from a sloping farmland soil in China, Environ. Sci. Pollut. R. 23 (2016) 995–1006.

[6] Z. Liu, B. Dugan, C.A. Masiello, H.M. Gonnermann, Biochar particle size, shape, and porosity act together to influence soil water properties, PLoS One 12 (6) (2017) e0179079https://doi.org/10.1371/journal.pone.0179079.

[7] S. Brunauer, P. Emmett, E. Teller, Adsorption of gases in multimolecular layers, J. Am. Chem. Soc. 60 (1938) 309–319.

[8] E. Barrett, L. Joyner, P. Halenda, The determination of pore volume and area distributions in porous substances. I. Computations from nitrogen isotherms, J. Am. Chem. Soc. 73 (1951) 373–380.

[9] M. Gray, M.G. Johnson, M.I. Dragila, M. Kleber, Water uptake in biochars: the roles of porosity and hydrophobicity, Biomass Bioener 61 (2014) 196–205.

[10] C. Brewer, V. Chuang, C. Masiello, H. Gonnermann, X. Gao, B. Dugan, L. Driver, P. Panzacchi, K. Zygourakis, C. Davies, New approaches to measuring biochar density and porosity, Biomass Bioenerg. 66 (2014) 176–185.

[11] J.B.W. Webber, P. Corbett, K.T. Semple, U. Ogbonnaya, W.S. Teel, C.A. Masiello, Q.J. Fisher, J.J. Valenza II, Y.-Q. Song, Q. Hu, An NMR study of porous rock and biochar containing organic material, Micropor. Mesopor. Mat. 178 (2013) 94–98.

[12] F.G.A. Verheijen, S. Jeffery, A.C. Bastos, M. van der Velde, I. Diafas, Biochar Application to Soils. A Critical Scientific Review of Effects on Soil Properties, Processes and Functions. EUR 24099 EN, Office for the Official Publications of the European Communities, Luxembourg, 2010, p. 149.

[13] M.I. Bird, P.L. Ascough, I.M. Young, C.V. Wood, A.C. Scott, X-ray microtomographic imaging of charcoal, J. Archaeol. Sci. 35 (2008) 2698–2706.

[14] P. Conte, N. Nestle, Water dynamics in different biochar fractions, Magn. Reson. Chem. 53 (2015) 726–734.

[15] S. Jeffery, M.B.J. Meinders, C.R. Stoof, T.M. Bezemer, T.F.J. van de Voorde, L. Mommer, J.W. van Groenigen, Biochar application does not improve the soil hydrological function of a sandy soil, Geoderma 251–252 (2015) 47–54.

[16] K. Jones, G. Ramakrishnan, M. Uchimiya, A. Orlov, New applications of X-ray tomography in pyrolysis of biomass: biochar imaging, Energ. Fuel. 29 (2015) 1628–1634.

[17] L.S. Schnee, S. Knauth, S. Hapca, W. Otten, T. Eickhorst, Analysis of physical pore space characteristics of two pyrolytic biochars and potential as microhabitat, Plant Soil 408 (2016) 357–368.

[18] J. Hyväluoma, S. Kulju, M. Hannula, H. Wikberg, A. Källi, K. Rasa, Quantitative characterization of pore structure of several biochars with 3D imaging, Environ. Sci. Pollut. Res. 25 (2018) 25648–25658.

[19] X. Yu, C. Wu, Y. Fu, P.C. Brookers, S. Lu, Three-dimensional pore structure and carbon distribution of macroaggregates in biochar-amended soil, Eur. J. Soil Sci. 67 (2016) 109–120.

[20] E. Turtola, A. Paajanen, Influence of improved subsurface drainage on phosphorus losses and nitrogen leaching from a heavy clay soil, Agric. Water Manag. 28 (1995) 295–310.

[21] P. Elonen, Particle-size analysis of soil, Acta Agral. Fenn. 122 (1971).

[22] G. Horgan, Mathematical morphology for analysing soil structure from images, Eur. J. Soil Sci. 49 (1998) 161–173.

[23] M. Hilpert, R. Glantz, C.T. Miller, Calibration of a pore-network model by a pore-morphological analysis, Transport Porous Med. 51 (2003) 267–285.

[24] M. Hilpert, C.T. Miller, Pore-morphology-based simulation of drainage in totally wetting porous media, Adv. Water Resour. 24 (2001) 243–255.

[25] Z. Tabor, E. Rokita, Quantifying anisotropy of trabecular bone from gray-level images, Bone 40 (2007) 966–972.

[26] J. Fromm, Hormonal physiology of wood growth in willow (*Salix viminalis* L.): effects of spermine and abscisic acid, Wood Sci. Technol. 31 (1997) 119–130.

[27] W. Schoch, J. Heller, F.H. Schweingruber, F. Kienast, Wood Anatomy of Central European Species, (2004) Online version: www.woodanatomy.ch.

[28] J. Hyväluoma, M. Hannula, K. Arstila, H. Wang, S. Kulju, K. Rasa, Effects of pyrolysis temperature on the hydrologically relevant porosity of willow biochar, J. Anal. Appl. Pyrol. https://doi.org/10.1016/j.jaap.2018.07.011.

[29] J. Ahrens, B. Geveci, C. Law, ParaView: an End-user Tool for Large Data Visualization, Visualization Handbook, Elsevier, 2005 ISBN-13: 978-0123875822.

[30] C.A. Schneider, W.S. Rasband, K.W. Eliceiri, NIH Image to ImageJ: 25 years of image analysis, Nat. Methods 9 (2012) 671–675.

[31] J. Park, I. Hung, Z. Gan, O. Rojas, K. Lim, S. Park, Activated carbon from biochar: influence of its physicochemical properties on the sorption characteristics of phenanthrene, Bioresour. Technol. 149 (2013) 383–389.

[32] J. Zhang, C. You, Water holding capacity and absorption properties of wood chars, Energ. Fuel. 27 (2013) 2643–2648.

[33] R.N. Wenzel, Resistance of solid surfaces to wetting by water, Ind. Eng. Chem. 28 (1936) 988–994.

[34] W. Suliman, J. Harsh, N. Abu-Lail, A. Fortuna, I. Dallmeyer, M. Garcia-Pérez, The role of biochar porosity and surface functionality in augmenting hydrologic properties of a sandy soil, Sci. Total Environ. 574 (2017) 139–147.

[35] G. Ojeda, S. Mattana, A. Àvila, J. Alcañiz, M. Volkmann, J. Bachmann, Are soil-water functions affected by biochar application? Geoderma 249–250 (2015) 1–11.

[36] S. Abel, A. Peters, S. Trinks, H. Schonsky, M. Facklam, G. Wessolek, Impact of biochar and hydrochar addition on water retention and water repellency of sandy soil, Geoderma 202–203 (2013) 183–191.

[37] T.J. Lim, K.A. Spokas, G. Feyereisen, J.M. Novak, Predicting impact of biochar additions on soil hydraulic conductivity, Chemosphere 142 (2016) 136–144.

[38] O.T. Denmead, R.H. Shaw, Availability of soil water to plants as affected by moisture content and meteorological conditions, Agron. J. 54 (1962) 385–390.

[39] W.S. Meyer, G.C. Green, Water use by wheat and plant indicators of available water, Agron. J. 72 (1980) 253–257.

[40] F.R. Rijsberman, Water scarcity: fact or fiction? Agric. Water Manag. 80 (2006) 5–22.

[41] N. Otsu, A threshold selection method from gray-level histograms, IEEE T. Syst. Man. Cyb. 9 (1979) 62–66.

[42] S.M. Hapca, A.N. Houston, W. Otten, P.C. Baveye, New local thresholding method for soil images by minimizing grayscale intra-class variance, Vadose Zone J. 12 (2013), https://doi.org/10.2136/vzj2012.0172.

[43] S. Svensson, G. Borgefors, Digital distance transforms in 3D images using information from neighbourhoods up to 5x5x5, Comput. Vis. Image Und. 88 (2002) 24–53.

[44] S. Succi, The Lattice Boltzmann Equation for Fluid Dynamics and beyond, Clarendon Press, Oxford, 2001, p. 288.

[45] J. Hyväluoma, V. Niemi, M. Thapaliya, E. Turtola, J. Järnstedt, J. Timonen, Lattice Boltzmann simulation of flow-induced wall shear stress in porous media, Transp. Por. Med. 121 (2018) 353–368.